Supporting Information

Ionic Liquid Exfoliated $Ti_3C_2T_x$ MXene Nanosheets for Photoacoustic Imaging and Synergistic Photothermal/Chemotherapy of Cancer

Beibei Lu,[a,b] Shunyou Hu,[a,b] Dong Wu,[a,b] Chengyu Wu,[a,b] Zhenye Zhu,[a,b] Lu Hu[c*] and Jiaheng Zhang[a,b*]

[a]Sauvage Laboratory for Smart Materials, Harbin Institute of Technology, Shenzhen 518055, P. R. China
[b]Research Centre of Printed Flexible Electronics, School of Materials Science and Engineering, Harbin Institute of Technology, Shenzhen 518055, P. R. China
[c]Guangdong Marubi Biotechnology Co., Ltd, Guangzhou 510000, P. R. China
E-mail: hu.lu@marubi.cn; zhangjiaheng@hit.edu.cn

1. Materials

Ti_3AlC_2 MAX powder (> 98 wt%) was purchased from Beike 2D Materials Co., Ltd. (Beijing, China). 1-Vinylimidazole, bromoethane, bromobutane, bromohexane, n-octyl bromide, 1-bromodecane, 1-bromododecane, 1-bromotetradecane, 1-bromohexadecane, and sodium tetrafluoroborate ($NaBF_4$) were obtained from Aldrich (Shanghai, China). Doxorubicin hydrochloride was obtained from Sigma-Aldrich (St. Louis, MO, USA). Cell counting kit-8 (CCK-8), Calcein-AM/propidium iodide (PI), and Annexin V-FITC apoptosis detection kits were purchased from Beyotime Biotechnology (Shanghai, China). Dulbecco's modified Eagle's medium (DMEM), fetal bovine serum (FBS), and trypsin-EDTA solution with phenol red were obtained from Gibco (Grand Island, NY, USA). 4% paraformaldehyde and 4, 6-diamidino-2-phenylindole (DAPI) were purchased from Solarbio (Beijing, China).

2. Characterization of IL exfoliated MXene

The chemical structures of the ILs dispersed in dimethyl sulfoxide-d_6 (DMSO-d_6) were analyzed by proton nuclear magnetic resonance (^{1}H NMR), carbon nuclear magnetic resonance (^{13}C NMR), and fluorine nuclear magnetic resonance (^{19}F NMR) spectroscopy (Bruker Avance III 400 MHz, USA). Fourier transform infrared (FTIR)

spectroscopy (Thermo Scientific Nicolet iS 50, USA) measurements of the ILs were carried out in the attenuated total reflectance mode. Structural and chemical analyses of the samples were performed using an X-ray photoelectron spectroscopy (XPS; Thermo ESCALAB 250Xi, USA) with a monochromatic Al Ka X-ray source. The XRD patterns were recorded using an X-ray diffractometer (Bruker D8, USA). Raman spectra were collected on a high-resolution analytical Raman microscopy (Horiba LabRAM HR80, Japan) using 532 nm laser excitation.

The morphology of MXene was characterized by scanning electron microscopy (SEM; 5 kV, Hitachi SU8010, Japan), transmission electron microscopy (TEM; 300 kV, FEI Tecnai G2 F30, Netherlands), and atomic force microscopy (AFM; Bruker Dimension Icon, USA). The size distribution and zeta potential of MXene in water were evaluated using a Zetasizer (Nano ZS, Malvern, UK). The transmittance of MXene was recorded on a UV-Vis-NIR spectrophotometer (Cary 5000, USA). Thermogravimetric analysis (TGA) was carried out in N_2 at a heating rate of 10 °C min^{-1} using a thermal analyzer (Netzsch STA 449F3, Germany). The specific heat capacity was measured by differential scanning calorimetry (DSC; Metler-Toledo, USA) using sapphire as the reference.

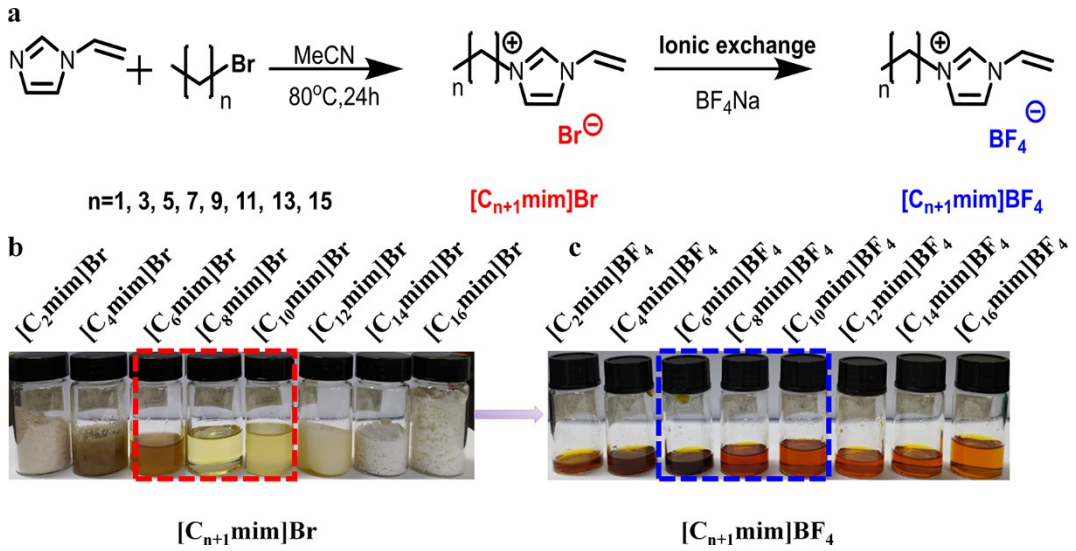

Figure S1. The synthetic scheme of $[C_{n+1}mim]BF_4$ ILs by ion exchange (a; n=1, 3, 5, 7, 9, 11, 13, 15). Digital photo of $[C_{n+1}mim]Br$ (b) and $[C_{n+1}mim]BF_4$ ILs (c).

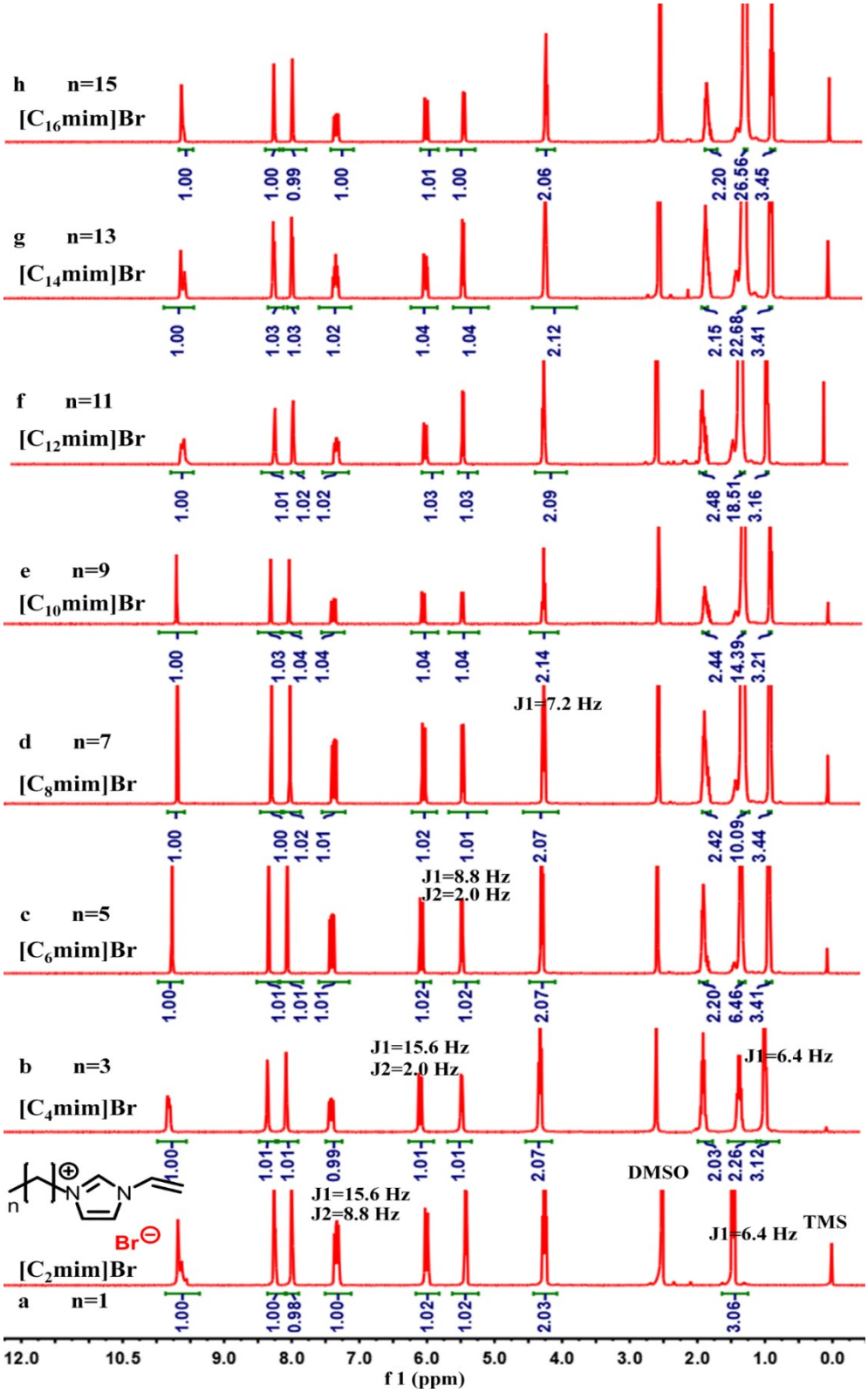

Figure S2. ^{1}H-NMR spectra of [C_{n+1}mim]Br ILs. (a) [C_2mim]Br (n=1), (b) [C_4mim]Br (n=3), (c) [C_6mim]Br (n=5), (d) [C_8mim]Br (n=7), (e) [C_{10}mim]Br (n=9), (f) [C_{12}mim]Br (n=11), (g) [C_{14}mim]Br (n=13), and (h) [C_{16}mim]Br (n=15).

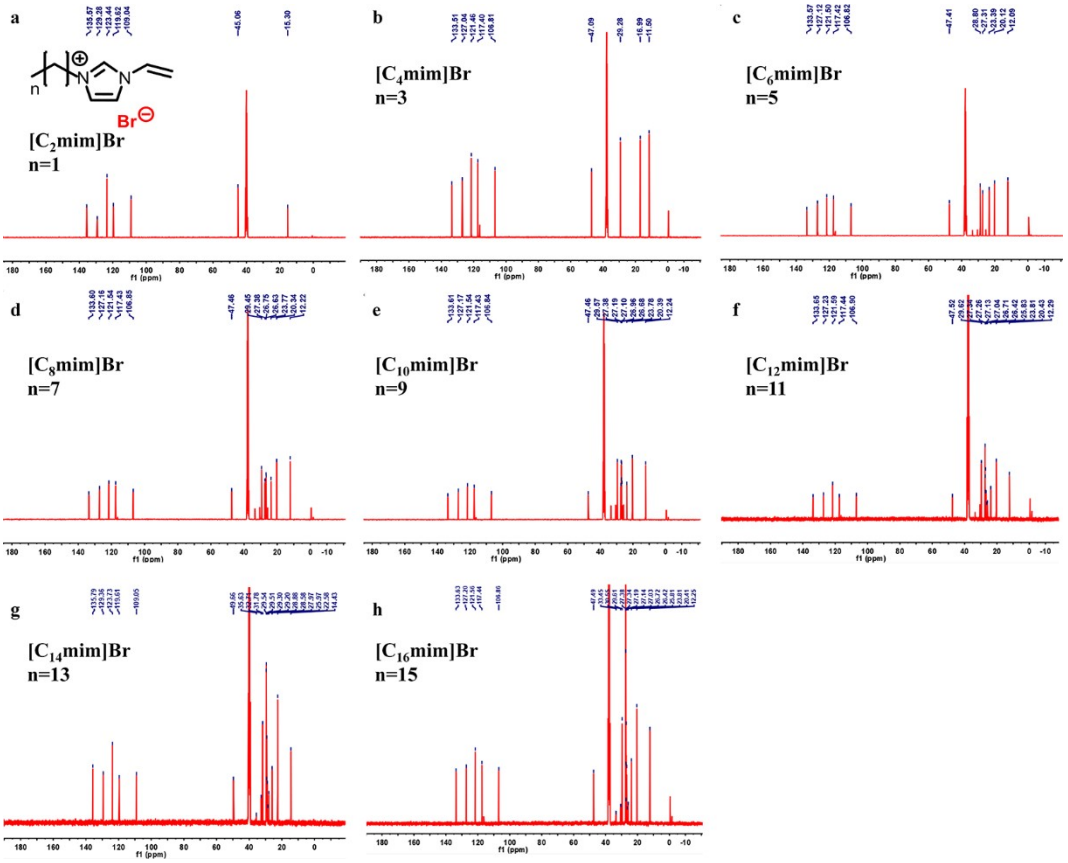

Figure S3. ^{13}C-NMR spectra of [C_{n+1}mim]Br ILs. (a) [C_2mim]Br (n=1), (b) [C_4mim]Br (n=3), (c) [C_6mim]Br (n=5), (d) [C_8mim]Br (n=7), (e) [C_{10}mim]Br (n=9), (f) [C_{12}mim]Br (n=11), (g) [C_{14}mim]Br (n=13), and (h) [C_{16}mim]Br (n=15).

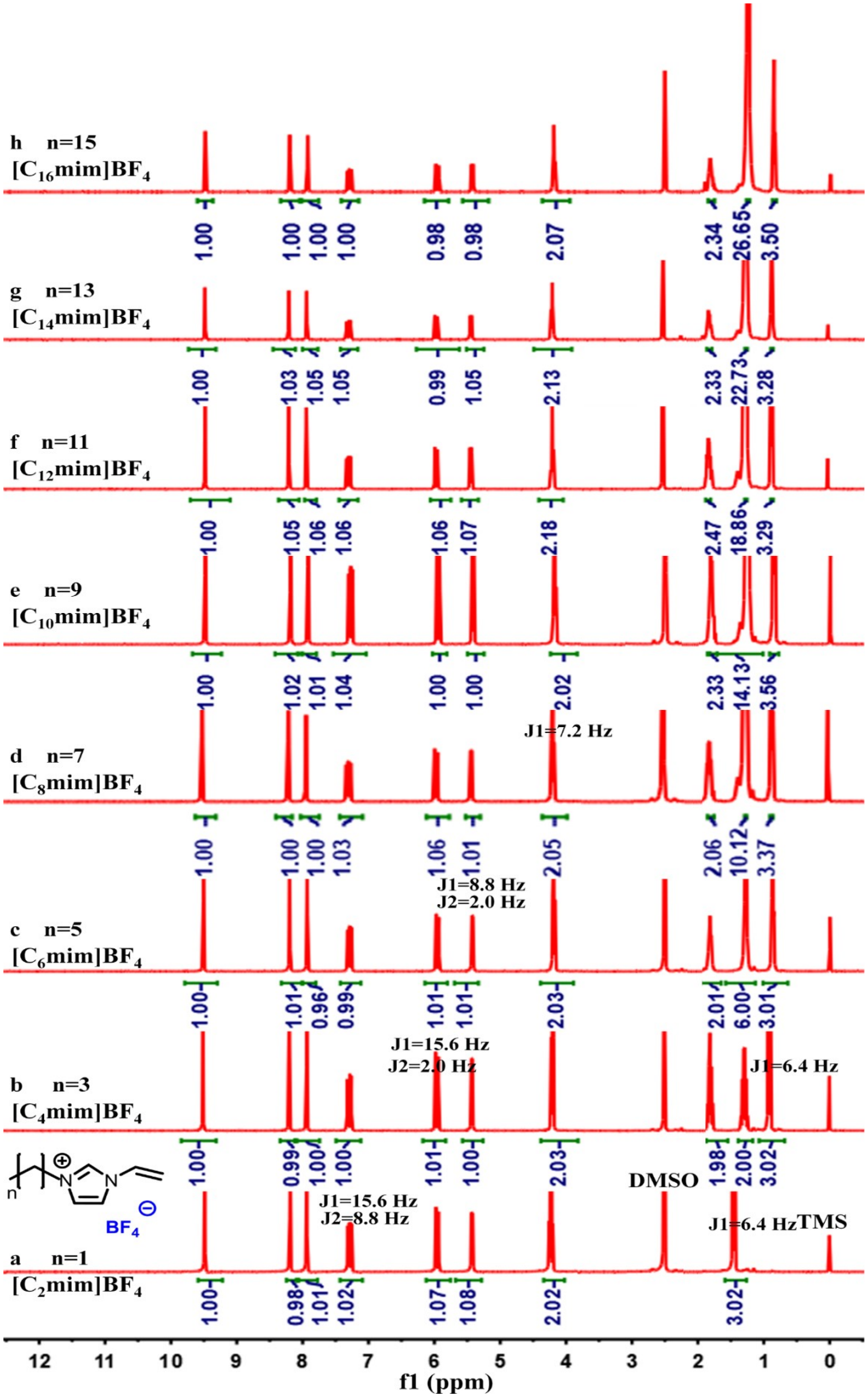

Figure S4. ^{1}H-NMR spectra of $[C_{n+1}mim]BF_4$ ILs. (a) $[C_2mim]BF_4$ (n=1), (b) $[C_4mim]BF_4$ (n=3), (c) $[C_6mim]BF_4$ (n=5), (d) $[C_8mim]BF_4$ (n=7), (e) $[C_{10}mim]BF_4$ (n=9), (f) $[C_{12}mim]BF_4$ (n=11), (g) $[C_{14}mim]BF_4$ (n=13), and (h) $[C_{16}mim]BF_4$

(n=15).

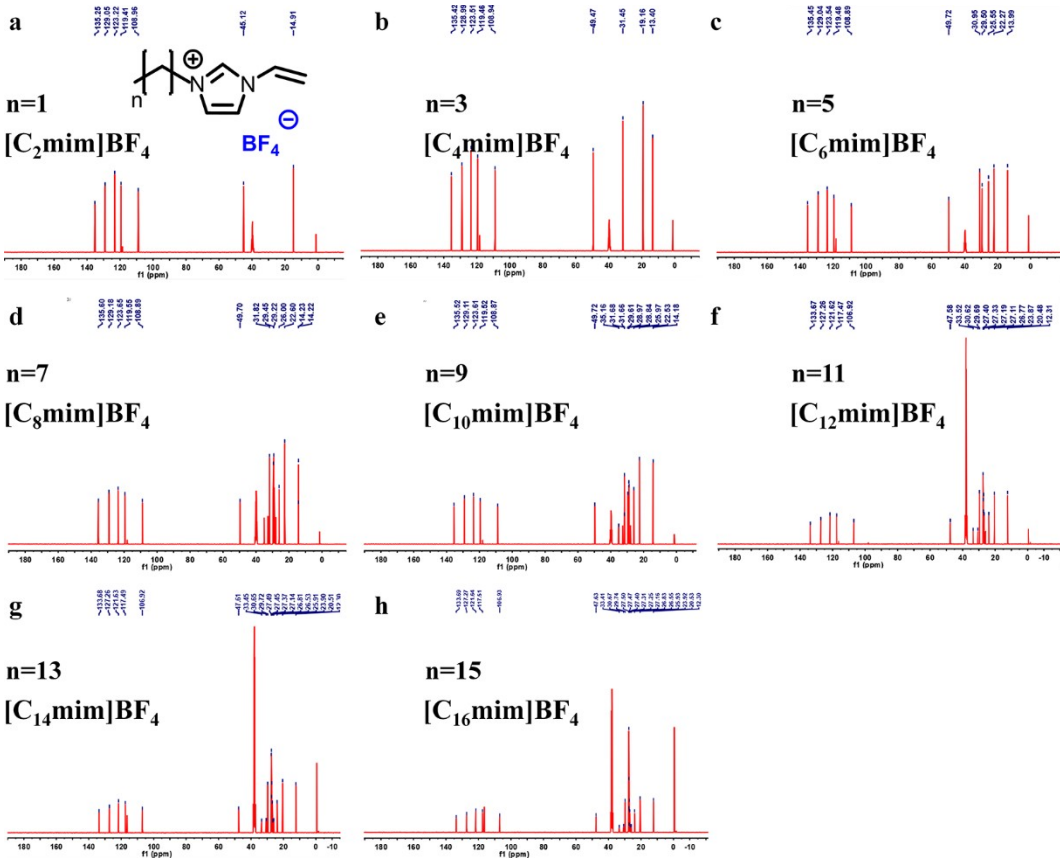

Figure S5. ^{13}C-NMR spectra of $[C_{n+1}mim]BF_4$ ILs. (a) $[C_2mim]BF_4$ (n=1), (b) $[C_4mim]BF_4$ (n=3), (c) $[C_6mim]BF_4$ (n=5), (d) $[C_8mim]BF_4$ (n=7), (e) $[C_{10}mim]BF_4$ (n=9), (f) $[C_{12}mim]BF_4$ (n=11), (g) $[C_{14}mim]BF_4$ (n=13), and (h) $[C_{16}mim]BF_4$ (n=15).

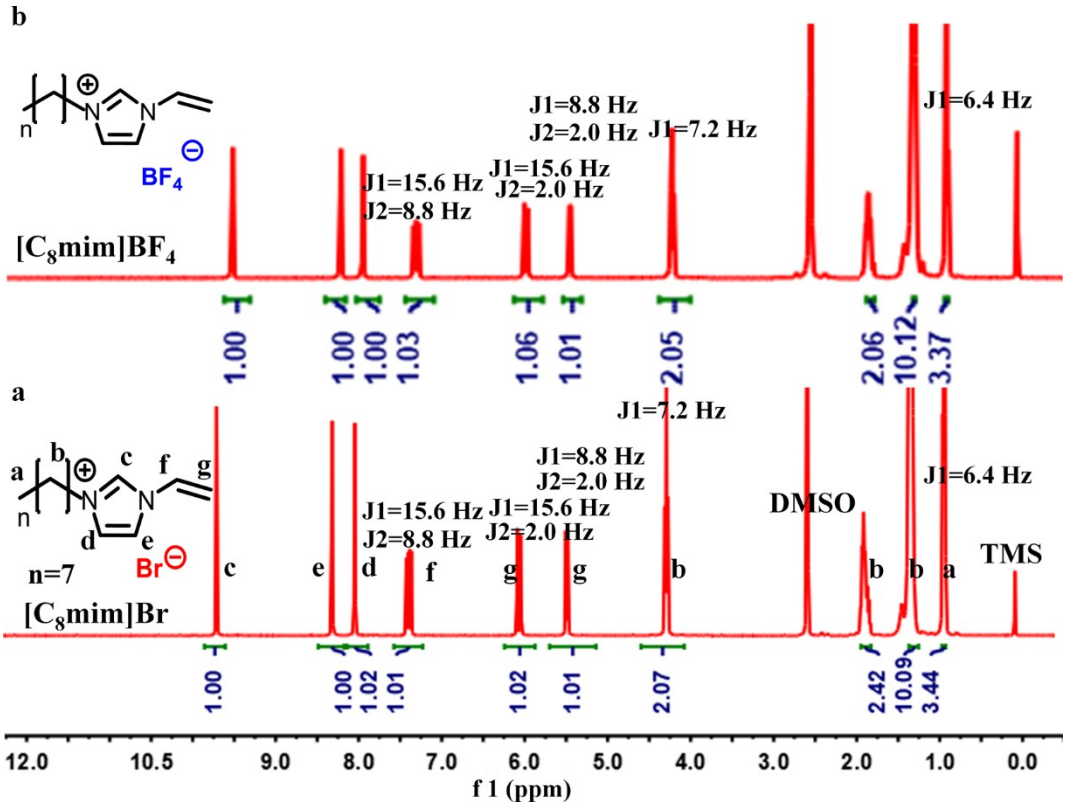

Figure S6. ^{1}H-NMR spectra of [C_8mim]Br and [C_8mim]BF_4 ILs (n=7).

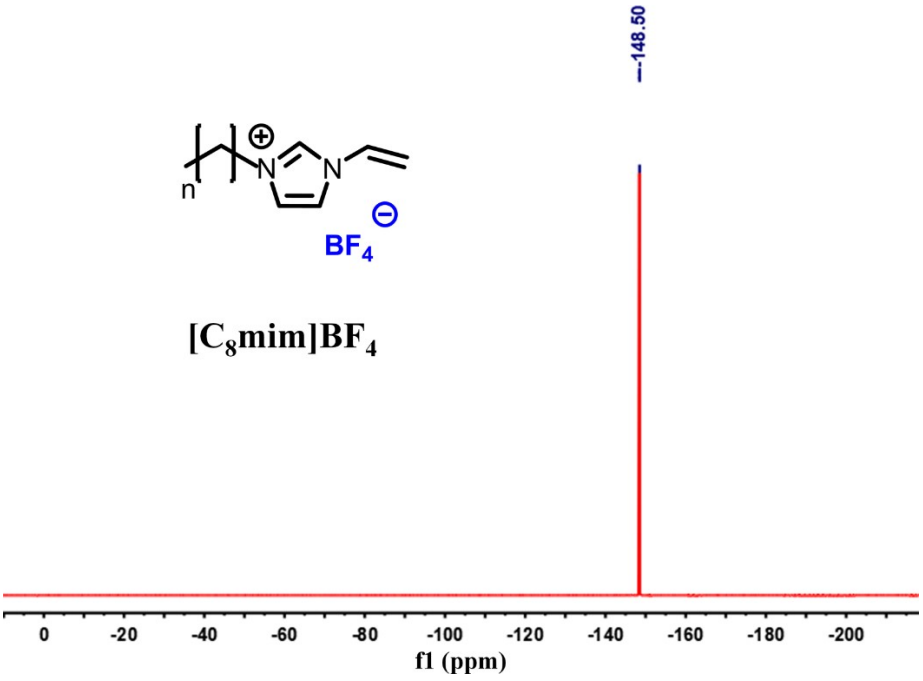

Figure S7. ^{19}F-NMR spectrum of [C_8mim]BF_4 ILs (n=7).

[C_2mim]Br, [C_4mim]Br, [C_6mim]Br, [C_8mim]Br, [C_{10}mim]Br, [C_{12}mim]Br, [C_{14}mim]Br, and [C_{16}mim]Br ILs were synthesized. The results of NMR (Figure S2 and Figure S3) and yields were as follows:[1,2]

[C_2mim]Br: White solid powder (yield: 98.15%). ^{1}HNMR (400 MHz, DMSO) δ (ppm): 9.70 (s, 1H), 8.27 (s, 1H), 8.02 (s, 1H), 7.34 (dd, 1H, J1=15.6 Hz, J2=8.8 Hz), 6.02 (dd, 1H, J1=15.6 Hz, J2=2.0 Hz), 5.43 (dd, 1H, J1=8.8 Hz, J2=2.0 Hz), 4.26 (t, 2H), 1.46 (t, 3H, J1=6.4 Hz). ^{13}C NMR (400 MHz, DMSO) δ (ppm): 135.57 (s), 129.28 (s), 123.44 (s), 119.62 (s), 109.04 (s), 45.06 (s), 15.30 (s).

[C_4mim]Br: Brown solid (yield: 97.63%). ^{1}HNMR (400 MHz, DMSO) δ (ppm): 9.81 (s, 1H), 8.34 (s, 1H), 8.05 (s, 1H), 7.39 (dd, 1H, J1=15.6 Hz, J2=8.8 Hz) 6.06 (dd, 1H, J1=15.6 Hz, J2=2.0 Hz), 5.44 (dd, 1H, J1=8.8 Hz, J2=2.0 Hz), 4.27 (t, 2H, J1=7.2 Hz), 1.84 (m, 2H), 1.30 (m, 2H), 0.92 (t, 3H, J1=6.4 Hz). ^{13}C NMR (400 MHz, DMSO) δ (ppm): 133.51 (s), 127.04 (s), 121.46 (s), 117.40 (s), 106.81 (s), 47.09 (s), 29.28 (s), 16.99 (s), 11.50 (s).

[C_6mim]Br: Brown viscous liquid (yield: 98.24%). ^{1}HNMR (400 MHz, DMSO) δ (ppm): 9.74 (s, 1H), 8.30 (s, 1H), 8.03 (s, 1H), 7.36 (dd, 1H, J1=15.6 Hz, J2=8.8 Hz), 6.03 (dd, 1H, J1=15.6 Hz, J2=2.0 Hz), 5.43 (dd, 1H, J1=8.8 Hz, J2=2.0 Hz), 4.24 (t, 2H, J1=7.2 Hz), 1.80 (m, 2H), 1.28 (m, 6H), 0.87 (t, 3H, J1=6.4Hz). ^{13}C NMR (400 MHz, DMSO) δ (ppm): 133.57 (s), 127.12 (s), 121.50 (s), 117.42 (s), 106.82 (s), 47.41 (s), 28.80 (s), 27.31 (s), 23.39 (s), 20.12 (s), 12.09 (s).

[C_8mim]Br: Light yellow viscous liquid (yield: 98.67%). ^{1}HNMR (400 MHz, DMSO) δ (ppm): 9.74 (s, 1H), 8.30 (s, 1H), 8.03 (s, 1H), 7.36 (dd, 1H, J1=15.6 Hz, J2=8.8 Hz), 6.03 (dd, 1H, J1=15.6 Hz, J2=2.0 Hz), 5.43 (dd, 1H, J1=8.8 Hz, J2=2.0 Hz), 4.24 (t, 2H, J1=7.2 Hz), 1.80 (m, 2H), 1.28 (m, 6H), 0.87 (t, 3H, J1=6.4 Hz). ^{13}C NMR (400 MHz, DMSO) δ (ppm): 133.60 (s), 127.16 (s), 121.54 (s), 117.43 (s), 106.85 (s), 47.46 (s), 29.45 (s), 27.38 (s), 26.75 (s), 26.63 (s), 23.77 (s), 20.34 (s), 12.22 (s).

[C_{10}mim]Br: Light yellow viscous liquid (yield: 97.62%). ^{1}HNMR (400 MHz, DMSO) δ (ppm): 9.68 (s, 1H), 8.27 (s, 1H), 8.00 (s, 1H), 7.34 (dd, 1H, J1=15.6 Hz, J2=8.8 Hz), 6.01 (dd, 1H, J1=15.6 Hz, J2=2.0 Hz), 5.43 (dd, 1H, J1=8.8 Hz, J2=2.0 Hz), 4.22 (t, 2H, J1=7.2 Hz), 1.801(m, 2H), 1.34 (m, 10H), 0.86 (t, 3H, J1=6.4 Hz). ^{13}C NMR (400 MHz, DMSO) δ (ppm): 133.61 (s), 127.17 (s), 121.54 (s), 117.43 (s), 106.84 (s), 47.46 (s), 29.57 (s), 27.38 (s), 27.19 (s), 27.10 (s), 26.96 (s), 26.68 (s), 23.78 (s), 20.39 (s), 12.24 (s).

[C_{12}mim]Br: White solid (yield: 95.48%). ^{1}HNMR (400 MHz, DMSO) δ (ppm): 9.64 (s, 1H), 8.26 (s, 1H), 8.00 (s, 1H), 7.33 (dd, 1H, J1=15.6 Hz, J2=8.8 Hz), 6.00 (dd, 1H, J1=15.6 Hz, J2=2.0 Hz), 5.43 (dd, 1H, J1=8.8 Hz, J2=2.0 Hz), 4.21 (t, 2H, J1=7.2 Hz), 1.82 (m, 2H), 1.24 (m, 18H), 0.85 (t, 3H, J1=6.4 Hz). ^{13}C NMR (400 MHz, DMSO) δ (ppm): 133.65 (s), 127.23 (s), 121.59 (s), 117.44 (s), 106.90 (s), 47.52 (s), 29.62 (s), 27.34 (s), 27.26 (s), 27.13 (s), 27.04 (s), 26.71 (s), 26.42 (s), 25.83 (s), 23.81 (s), 20.43 (s), 12.29 (s).

[C_{14}mim]Br: White solid powder (yield: 93.72%). ^{1}HNMR (400 MHz, DMSO) δ (ppm): 9.60 (s, 1H), 8.24 (s, 1H), 7.97 (s, 1H), 7.32 (dd, 1H, J1=15.6 Hz, J2=8.8 Hz), 5.98 (dd, 1H, J1=15.6 Hz, J2=2.0 Hz), 5.43 (dd, 1H, J1=8.8 Hz, J2=2.0 Hz), 4.22 (t, 2H, J1=7.2 Hz), 1.80 (m, 2H), 1.24 (m, 22H), 0.85 (t, 3H, J1=6.4 Hz). ^{13}C NMR (400 MHz, DMSO) δ (ppm): 135.79 (s), 129.36 (s), 123.73 (s), 119.61 (s), 109.05 (s), 49.66 (s), 35.63 (s), 32.71 (s), 31.78 (s), 29.54 (s), 29.51 (s), 29.30 (s), 29.20 (s), 28.88 (s), 28.58 (s), 27.97 (s), 25.97 (s), 22.58 (s), 14.43 (s).

[C_{16}mim]Br: White solid powder (yield: 95.60%). ^{1}HNMR (400 MHz, DMSO) δ (ppm): 9.61 (s, 1H), 8.25 (s, 1H), 7.98 (s, 1H), 7.33 (dd, 1H, J1=15.6 Hz, J2=8.8 Hz), 5.99 (dd, 1H, J1=15.6 Hz, J2=2.0 Hz), 5.43 (dd, 1H, J1=8.8 Hz, J2=2.0 Hz), 4.21 (t, 2H, J1=7.2 Hz), 1.80 (m, 2H), 1.24 (m, 26H), 0.85 (t, 3H, J1=6.4 Hz). ^{13}C NMR (400 MHz, DMSO) δ (ppm): 133.63.79 (s), 127.20 (s), 121.56 (s), 117.44 (s), 106.86 (s),

47.49 (s), 33.45 (s), 30.55 (s), 29.61 (s), 27.38 (s), 27.34 (s), 27.19 (s), 27.14 (s), 27.03 (s), 26.72 (s), 26.42 (s), 25.81 (s), 23.81 (s), 20.41 (s), 12.25 (s).

$[C_2mim]BF_4$, $[C_4mim]BF_4$, $[C_6mim]BF_4$, $[C_8mim]BF_4$, $[C_{10}mim]BF_4$, $[C_{12}mim]BF_4$, $[C_{14}mim]BF_4$, and $[C_{16}mim]BF_4$ ILs were synthesized by ionic exchange. The results of NMR (Figure S4 and Figure S5) and yields were as follows:

$[C_2mim]BF_4$: Dark brown viscous liquid (yield: 94.13%). ^{1}HNMR (400 MHz, DMSO) δ (ppm): 9.49 (s, 1H), 8.19 (s, 1H), 7.94 (s, 1H), 7.29 (dd, 1H, J1=15.6 Hz, J2=8.8 Hz), 5.96 (dd, 1H, J1=15.6 Hz, J2=2.0 Hz), 5.43 (dd, 1H, J1=8.8 Hz, J2=2.0 Hz), 4.23 (t, 2H, J1=7.2 Hz), 1.46 (t, 3H, J1=6.4 Hz). ^{13}C NMR (400 MHz, DMSO) δ (ppm): 135.25 (s), 129.05 (s), 123.22 (s), 119.41 (s), 108.96 (s), 45.12 (s), 14.91 (s).

$[C_4mim]BF_4$: Brown viscous liquid (yield: 93.21%). ^{1}HNMR (400 MHz, DMSO) δ (ppm): 9.51 (s, 1H), 8.20 (s, 1H), 7.93(s, 1H), 7.29 (dd, 1H, J1=15.6 Hz, J2=8.8 Hz), 5.96 (dd, 1H, J1=15.6 Hz, J2=2.0 Hz), 5.43 (dd, 1H, J1=8.8 Hz, J2=2.0 Hz), 4.21 (t, 2H, J1=7.2 Hz), 1.81 (m, 2H), 1.27 (m, 2H), 0.92 (t, 3H, J1=6.4 Hz). ^{13}C NMR (400 MHz, DMSO) δ (ppm): 133.42 (s), 128.99 (s), 123.51 (s), 119.46 (s), 108.94 (s), 49.47 (s), 31.35 (s), 19.16 (s), 13.40 (s).

$[C_6mim]BF_4$: Brown viscous liquid (yield: 97.85%). ^{1}HNMR (400 MHz, DMSO) δ (ppm): 9.51 (s, 1H), 8.20 (s, 1H),7.95 (s, 1H), 7.29 (dd, 1H, J1=15.6 Hz, J2=8.8 Hz), 5.96 (dd, 1H, J1=15.6 Hz, J2=2.0 Hz), 5.43 (dd, 1H, J1=8.8 Hz, J2=2.0 Hz), 4.19 (t, 2H, J1=7.2 Hz), 1.81 (m, 2H), 1.28 (m, 6H), 0.87 (t, 3H, J1=6.4 Hz). ^{13}C NMR (400 MHz, DMSO) δ (ppm): 135.45 (s), 129.04 (s), 123.54 (s), 119.48 (s), 108.89 (s), 49.72 (s), 30.95 (s), 29.50 (s), 25.55 (s), 22.27 (s), 13.99 (s).

$[C_8mim]BF_4$: Light brown viscous liquid (yield: 96.78%). ^{1}HNMR (400 MHz, DMSO) δ (ppm): 9.52 (s, 1H), 8.21 (s, 1H), 7.94 (s, 1H), 7.29 (dd, 1H, J1=15.6 Hz, J2=8.8

Hz), 5.96 (dd, 1H, J1=15.6 Hz, J2=2.0 Hz), 5.43 (dd, 1H, J1=8.8 Hz, J2=2.0 Hz), 4.19 (t, 2H, J1=7.2 Hz), 1.75 (m, 2H), 1.34 (m, 6H), 0.86 (t, 3H, J1=6.4 Hz). ^{13}C NMR (400 MHz, DMSO) δ (ppm): 135.60 (s), 129.18 (s), 123.65 (s), 119.55 (s), 108.89 (s), 49.70 (s), 31.82 (s), 29.45 (s), 29.22 (s), 26.00 (s), 22.60 (s), 14.23 (s), 14.22 (s). ^{19}F NMR (400 MHz, DMSO) δ (ppm): -148.50 (s).

[C_{10}mim]BF_4: Light brown viscous liquid (yield: 95.34%). ^{1}HNMR (400 MHz, DMSO) δ (ppm): 9.49 (s, 1H), 8.20 (s, 1H), 7.93 (s, 1H), 7.29 (dd, 1H, J1=15.6 Hz, J2=8.8 Hz), 5.95 (dd, 1H, J1=15.6 Hz, J2=2.0 Hz), 5.43 (dd, 1H, J1=8.8 Hz, J2=2.0 Hz), 4.19 (t, 2H, J1=7.2 Hz), 1.80 (m, 2H), 1.30 (m, 10H), 0.86 (t, 3H, J1=6.4 Hz). ^{13}C NMR (400 MHz, DMSO) δ (ppm): 135.52 (s), 129.11 (s), 123.61 (s), 119.52 (s), 108.87 (s), 49.72 (s), 35.16 (s), 31.68 (s), 3.66 (s), 29.61 (s), 28.87 (s), 28.84 (s), 25.97 (s), 22.53 (s), 14.18 (s).

[C_{12}mim]BF_4: Light brown viscous liquid (yield: 94.63%). ^{1}HNMR (400 MHz, DMSO) δ (ppm): 9.47 (s, 1H), 8.20 (s, 1H), 7.93 (s, 1H), 7.28 (dd, 1H, J1=15.6 Hz, J2=8.8 Hz), 5.95 (dd, 1H, J1=15.6 Hz, J2=2.0 Hz), 5.43 (dd, 1H, J1=8.8 Hz, J2=2.0 Hz), 4.19 (t, 2H, J1=7.2Hz), 1.79 (m, 2H), 1.24 (m, 18H), 0.86 (t, 3H, J1=6.4 Hz). ^{13}C NMR (400 MHz, DMSO) δ (ppm): 133.67 (s), 127.26 (s), 121.62 (s), 117.47 (s), 106.92 (s), 47.58 (s), 33.52 (s), 30.62 (s), 29.69 (s), 27.40 (s), 27.33 (s), 27.19 (s), 27.11 (s), 26.77 (s), 23.87 (s), 20.48 (s), 12.31 (s).

[C_{14}mim]BF_4: Light brown viscous liquid (yield: 92.45%). ^{1}HNMR (400 MHz, DMSO) δ (ppm): 9.47 (s, 1H), 8.19 (s, 1H), 7.92 (s, 1H), 7.29 (dd, 1H, J1=15.6 Hz, J2=8.8 Hz), 5.95 (dd, 1H, J1=15.6 Hz, J2=2.0 Hz), 5.42 (dd, 1H, J1=8.8 Hz, J2=2.0 Hz), 4.19 (t, 2H, J1=7.2 Hz), 1.78 (m, 2H), 1.24 (m, 22H), 0.84 (t, 3H, J1=6.4 Hz). ^{13}C NMR (400 MHz, DMSO) δ (ppm): 133.68 (s), 127.26 (s), 121.63 (s), 117.49 (s), 106.92 (s), 47.61 (s), 33.45 (s), 30.65 (s), 29.72 (s), 27.49 (s), 27.45 (s), 27.37 (s), 27.14 (s), 26.81 (s), 26.53 (s), 25.91 (s), 23.90 (s), 20.51 (s), 12.30 (s).

[C_{16}mim]BF_4: Light brown viscous liquid (yield: 93.48%). ^{1}HNMR (400 MHz, DMSO) δ (ppm): 9.46 (s, 1H), 8.19 (s, 1H), 7.91 (s, 1H), 7.28 (dd, 1H, J1=15.6 Hz, J2=8.8 Hz), 5.95 (dd, 1H, J1=15.6 Hz, J2=2.0 Hz), 5.42 (dd, 1H, J1=8.8 Hz, J2=2.0 Hz), 4.19 (t, 2H, J1=7.2 Hz), 1.77 (m, 2H), 1.24 (m, 26H), 0.86 (t, 3H, J1=6.4 Hz). ^{13}C NMR (400 MHz, DMSO) δ (ppm): 133.69 (s), 127.27 (s), 121.64 (s), 117.64 (s), 106.93 (s), 47.63 (s), 33.41 (s), 30.67 (s), 29.74 (s), 27.50 (s), 27.47 (s), 27.40 (s), 27.31 (s), 27.25 (s), 27.16 (s), 26.83 (s), 26.55 (s), 25.93 (s), 23.92 (s), 20.53 (s), 12.30 (s).

Besides, it can be seen from Figure S8a,b that the ILs contain obvious C-H stretching vibration (2927 cm^{-1}), C=C stretching peak (1662 cm^{-1}), and C-F absorption peak (1030 cm^{-1}), indicating that [C_{n+1}mim]BF_4 ILs has been successfully prepared using NMR and FTIR spectra.[3]

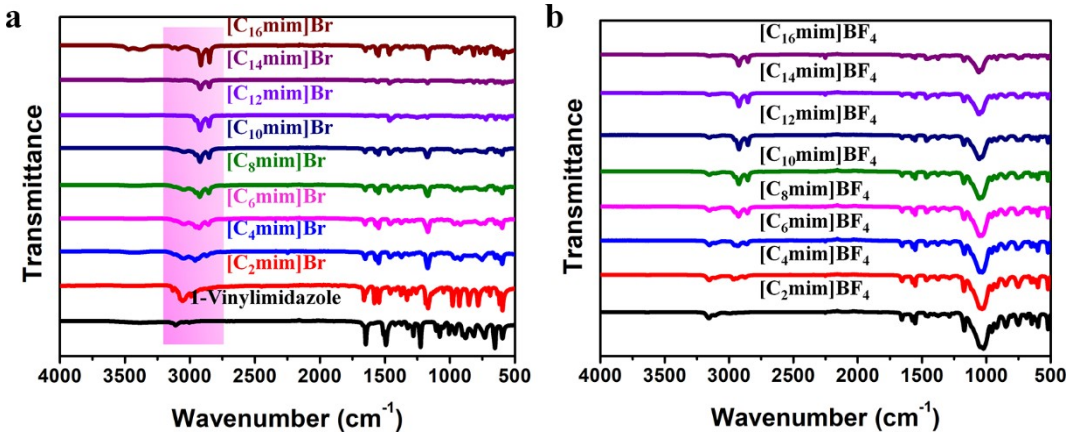

Figure S8. FTIR spectra of [C_{n+1}mim]Br (a) and [C_{n+1}mim]BF_4 ILs (b).

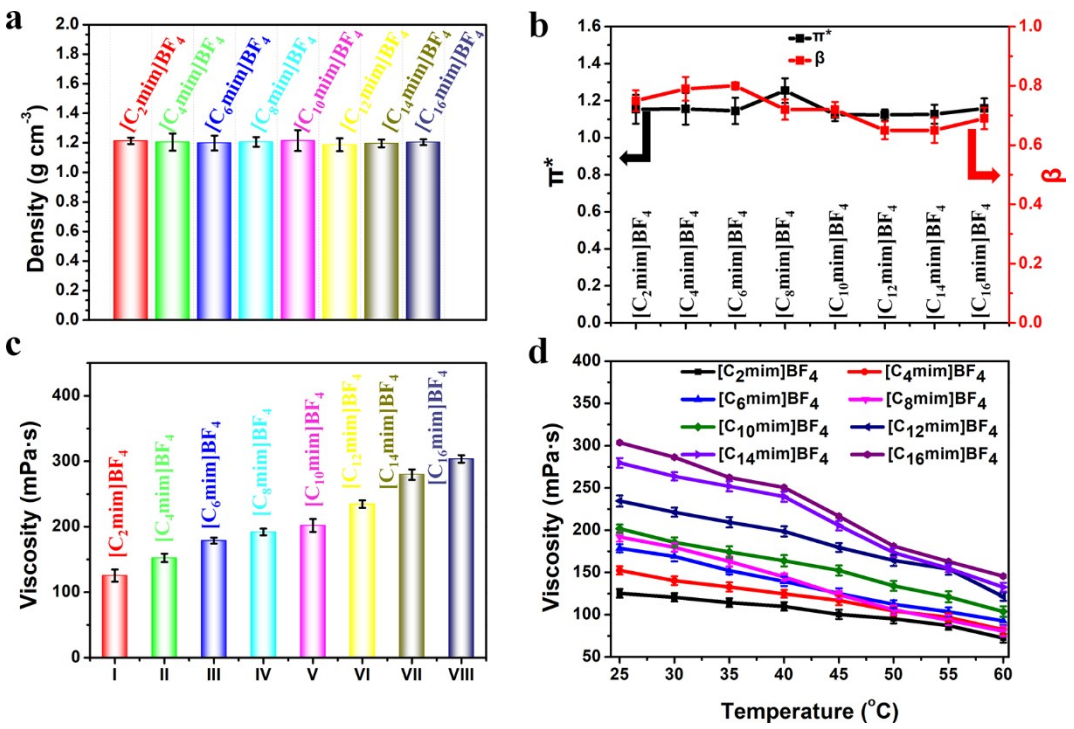

Figure S9. Physico-chemical properties of $[C_{n+1}mim]BF_4$ ILs. (a) Density of the $[C_{n+1}mim]BF_4$ at 25 ℃ (n=3). (b) Kamlet-Taft parameters: dipolarity/polarizability (π*) and hydrogen-bond basicity (β) of the $[C_{n+1}mim]BF_4$ ILs at 25 ℃ (n=3). (c) Viscosity of the $[C_{n+1}mim]BF_4$ ILs at 25 ℃ and (d) different temperature (n=3).

With the increase of the carbon chain, there was no obvious change in density (Figure S9a). As we all know, the polarity of the solvent will significantly affect the entire reaction process. $[C_{n+1}mim]BF_4$ ILs have strong hydrogen bond alkalinity, β value was approximately 0.6–0.8 (Figure S9b). This was because the basic properties of IL can be effectively enhanced by reducing the interaction between cations and anions. Bipolar/polarizability (π*) showed a relatively high value (1.0~1.4). Considering that polar molecular solvents usually have a high π* value, these $[C_{n+1}mim]BF_4$ greatly enhance the affinity for weakly polar biologically active compounds. The viscosity of $[C_{n+1}mim]BF_4$ ILs with different molar ratios was approximately 100–300 mPa·s at 25 ℃ (Figure S9c and Table S1). Interestingly, with the increase of the carbon chain, the viscosity of $[C_{n+1}mim]BF_4$ ILs increases; while the temperature increases, the viscosity gradually decreases (Figure S9d and Table S1).

According to the literature, Kamlet-Taft parameters, hydrogen bond basicity (β), and bipolarity/polarizability (π*) were measured using solvatochromic experiments. First, dissolve an appropriate amount of probe molecules (4-nitroaniline (NA) and N, N-diethyl-4-nitroaniline (DENA)) into the $[C_{n+1}mim]BF_4$ ILs aqueous solution sample, and then the mixture. Next, record the maximum absorption wavelength (λ_{max}) at 25 °C using UV-vis (PerkinElmer, Lambda 365, USA). Each sample was repeated at least three times and taken the average. The Kamlet-Taft dipolarity/polarizability π* and hydrogen bond basicity β were calculated using the following equations:[4,5]

$$\pi^* = 8.649 - 0.314 \times \lambda_{DENA} \qquad (1)$$

$$\beta = -0.357 \times \lambda_{NA} - 1.176 \times \pi^* + 11.12 \qquad (2)$$

where λ_{DENA} and λ_{NA} were the maximum absorption values of N, N-diethyl-4-nitroaniline, and 4-nitroaniline, respectively.

Table S1. Viscosity (mPa·s) of $[C_{n+1}mim]BF_4$ ILs at different temperatures (n=3).

ILs	Temperature (℃)							
	25 ℃	30 ℃	35 ℃	40 ℃	45 ℃	50 ℃	55 ℃	60 ℃
$[C_2mim]BF_4$	125.36±5.1	120.62±4.85	114.3±5.02	109.85±4.96	100.36±5.42	95.26±5.56	87.14±4.89	72.36±5.16
$[C_4mim]BF_4$	152.46±4.98	140.26±5.16	132.85±5.45	124.75±4.64	116.8±5.42	104.45±5.61	96.75±4.89	82.31±5.62
$[C_6mim]BF_4$	178.65±4.78	168.95±5.65	152.34±4.89	139.45±5.45	125.06±6.06	112.34±4.64	103.47±5.14	92.64±5.06
$[C_8mim]BF_4$	192.03±5.65	179.68±4.74	163.02±5.98	144.75±4.06	123.64±4.41	105.78±5.28	93.46±5.96	80.42±6.16
$[C_{10}mim]BF_4$	201.78±5.01	185.69±5.95	174.2±6.75	163.84±6.64	152.48±5.96	134.2±5.85	121.14±6.45	103.67±6.26
$[C_{12}mim]BF_4$	234.56±6.56	221.36±5.42	209.41±6.06	198.62±5.98	179.56±5.15	164.23±6.46	154.03±6.78	121.46±5.04
$[C_{14}mim]BF_4$	279.63±5.64	263.75±4.85	252.03±5.97	239.78±6.03	205.46±5.75	173.52±5.42	154.75±4.56	132.63±5.14
$[C_{16}mim]BF_4$	303.64±4.75	286.42±5.68	262.34±6.42	250.47±5.98	216.48±6.31	181.06±5.02	162.78±4.78	145.64±5.64

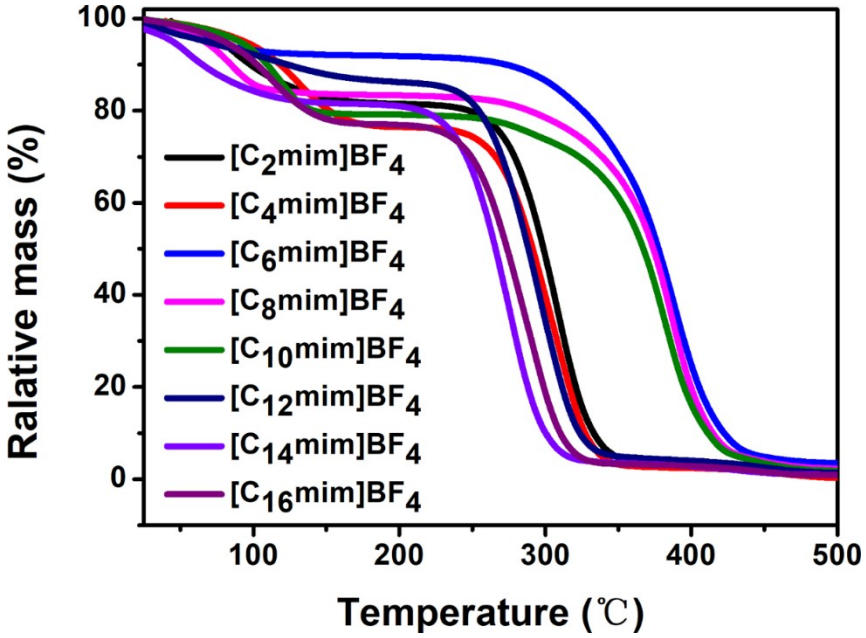

Figure S10. TGA analysis of $[C_{n+1}mim]BF_4$ ILs.

Table S2. Thermal stability properties of each of the variants $[C_{n+1}mim]BF_4$ ILs, including the temperature of decomposition (T_{dec}) and glass transition temperature (T_g).

Sample	T_{dec} (℃)	T_g (℃) [a]
$[C_2mim]BF_4$	255.10	/
$[C_4mim]BF_4$	248.15	/
$[C_6mim]BF_4$	291.45	/
$[C_8mim]BF_4$	303.56	/
$[C_{10}mim]BF_4$	300.08	/
$[C_{12}mim]BF_4$	243.87	/
$[C_{14}mim]BF_4$	248.15	/
$[C_{16}mim]BF_4$	230.86	/

a: No featuring DSC peaks above −50 °C

The thermal stability of IL is very important in drug delivery. The thermal stability of IL was determined using thermogravimetric analysis (TGA, Figure S10) and differential scanning calorimetry (DSC, Table S2). It can be seen that as the carbon chain increases, the thermal decomposition temperature (T_{dec}) also first increases and then decreases. Surprisingly, $[C_8mim]BF_4$ has the highest T_{dec} and the best stability.

Besides, the glass transition temperature (T_g) of $[C_{n+1}mim]BF_4$ were less than -50 ℃, as shown in Table S2. Therefore, $[C_6mim]BF_4$, $[C_8mim]BF_4$, and $[C_{10}mim]BF_4$ ILs have good stability, and we choose it for subsequent MAX stripping for the following experiments.

$[C_6mim]BF_4$, $[C_8mim]BF_4$, and $[C_{10}mim]BF_4$ ILs exfoliated the MAX phase. AFM images were shown in Figure 1d and Figure S12. Statistical analysis showed that the average lateral size and thickness are approximately lower than 200 nm and 1-5 nm (Figure S11), respectively. It should be noted that the $[C_8mim]BF_4$ stripped MAX nanosheets were better than the $[C_6mim]BF_4$ and $[C_{10}mim]BF_4$. In addition, we tested the toxicity of $[C_{n+1}mim]BF_4$ ILs (Figure S13) and found that with the increase of carbon chain and concentration, $[C_{n+1}mim]BF_4$ ILs have inhibition of 4T1 cells (Figure S13a), but they did not kill L929 (normal cells, Figure S13b). Therefore, this also verified that the IL itself has a certain ability to inhibit tumor growth. We chose $[C_8mim]BF_4$ to exfoliate the MAX phase for the subsequent photothermal and cell uptake experiments.

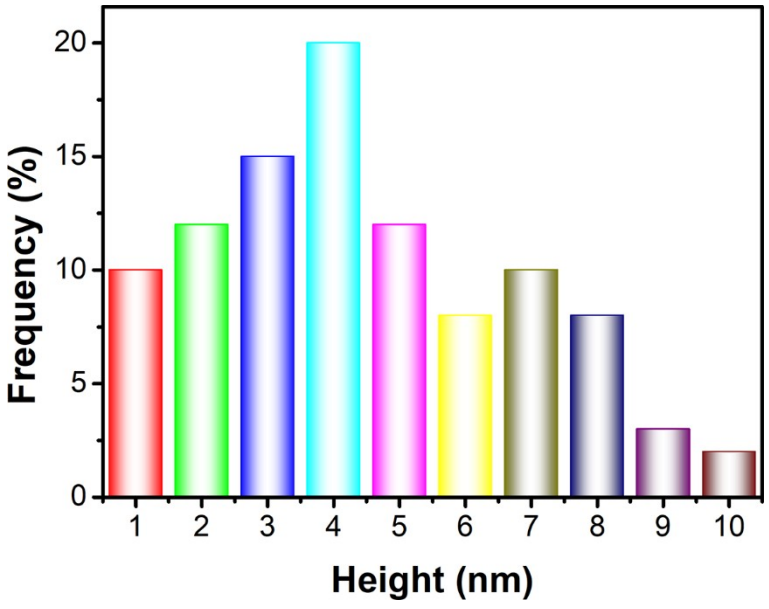

Figure S11. Typical height profiles statistics of $[C_8mim]BF_4$ ILs.

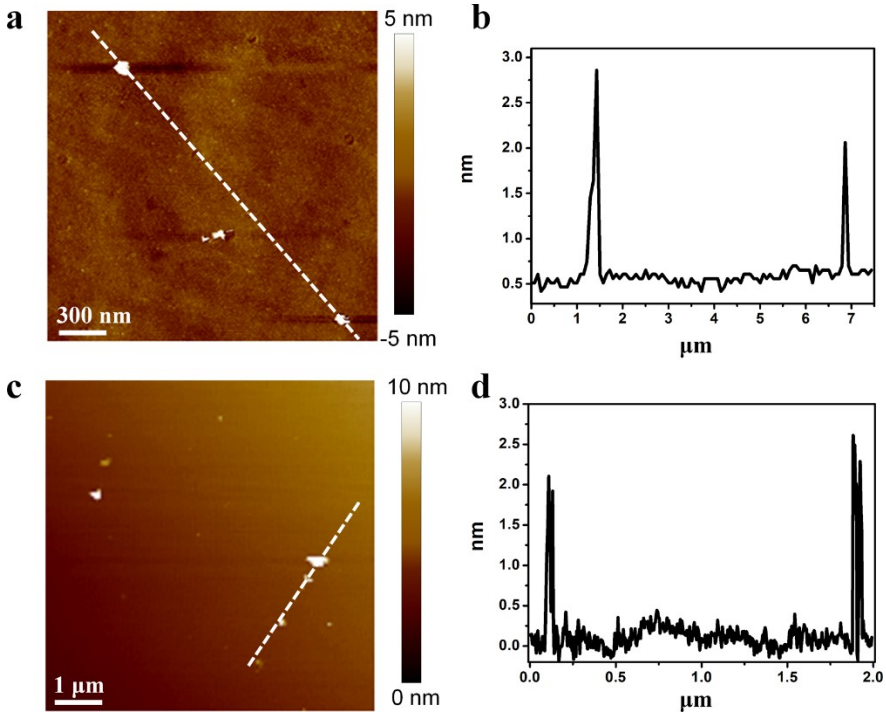

Figure S12. AFM image and typical height profiles of $[C_6mim]BF_4$ (a-b) and $[C_{10}mim]BF_4$ ILs (c-d).

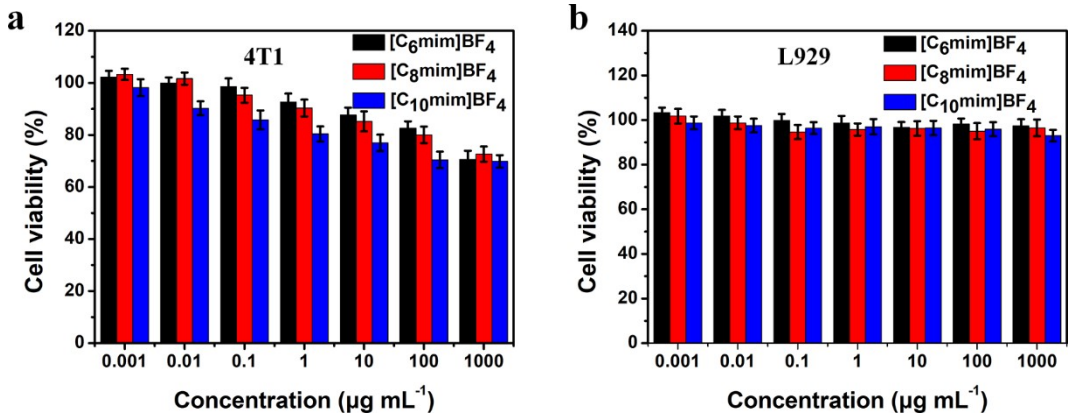

Figure S13. Cell cytotoxicity of $[C_6mim]BF_4$, $[C_8mim]BF_4$, and $[C_{10}mim]BF_4$ ILs against 4T1 (a) and L929 (b) cells after 24 h incubation (n=6).

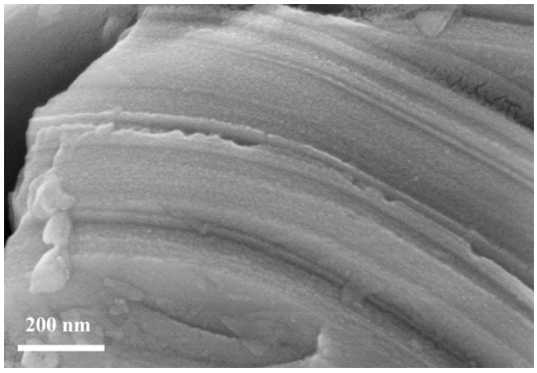

Figure S14. SEM image of Ti_3AlC_2 MAX before etching.

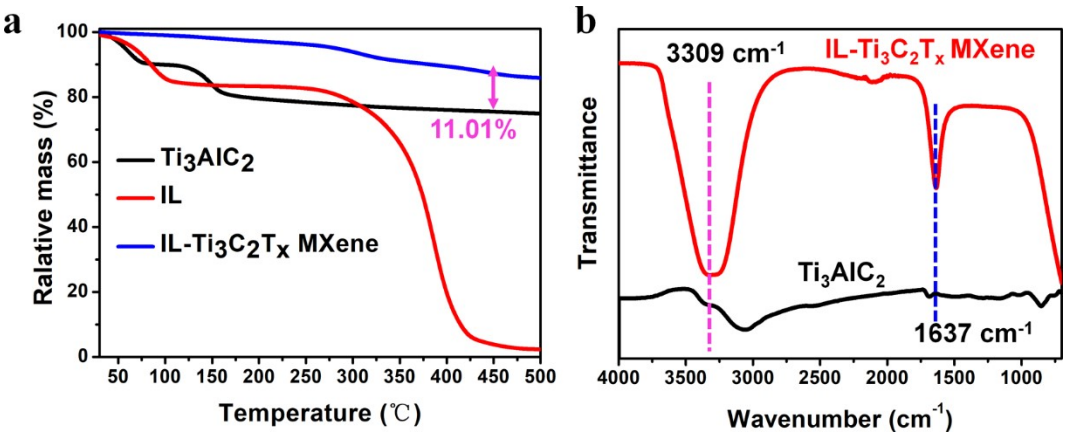

Figure S15. (a) TGA analysis and (b) FTIR spectra of Ti_3AlC_2 and IL-$Ti_3C_2T_x$ MXene nanosheets.

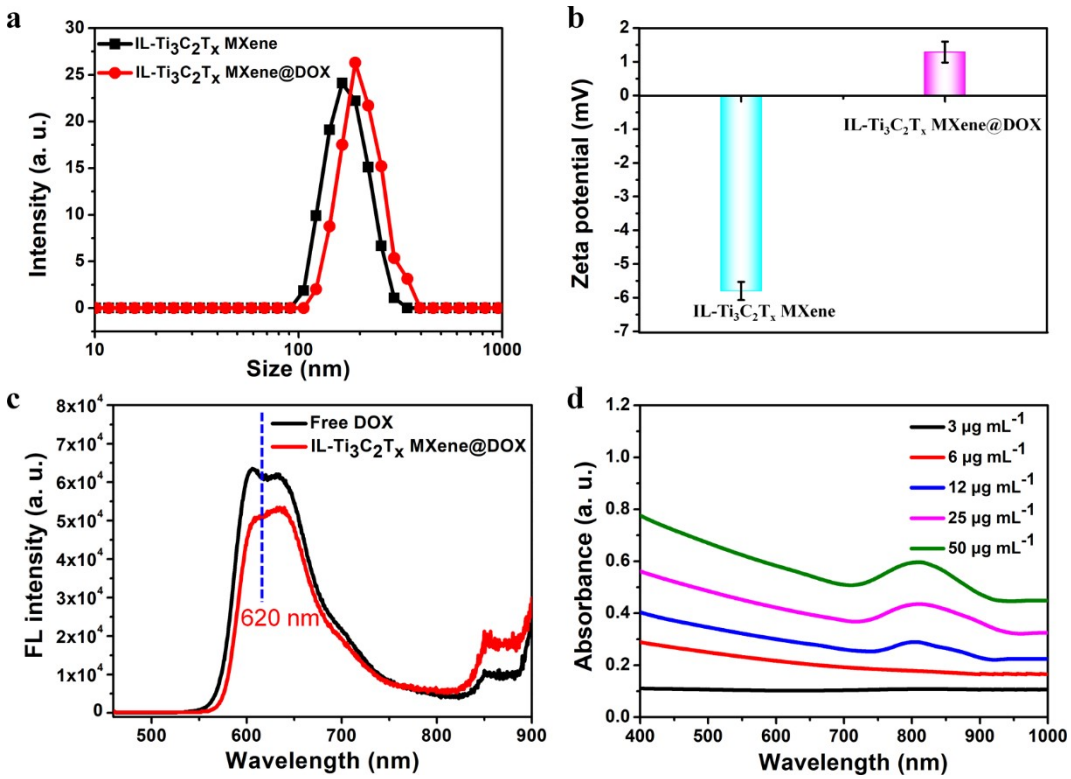

Figure S16. (a) Dynamic light scattering (DLS) profile and zeta potentials (b) of IL-$Ti_3C_2T_x$ MXene and IL-$Ti_3C_2T_x$ MXene@DOX nanocomposites in water solutions (n=3). (c) Fluorescence spectra of free DOX and IL-$Ti_3C_2T_x$ MXene@DOX nanocomposites in water solutions. (d) UV-vis-NIR absorption spectra of IL-$Ti_3C_2T_x$ MXene nanosheets at different concentrations.

Table S3. The size and zeta potential of IL-$Ti_3C_2T_x$ MXene were measured by DLS (n=3).

Group	Size (nm)	Zeta potential (mV)
H_2O	164.5±3.96	-5.8±0.27
PBS	142.3±2.16	-7.07±0.15
Saline	122.8±4.15	-5.22±0.36
DMEM	114.6±2.06	-8.35±0.22

Table S4. The size of the IL-$Ti_3C_2T_x$ MXene was measured by DLS (n=3).

Group	Size (nm)	Zeta potential (mV)
IL-$Ti_3C_2T_x$ MXene	164.5±3.96	-5.8±0.27
IL-$Ti_3C_2T_x$ MXene@DOX	191.4±3.25	1.29±0.31

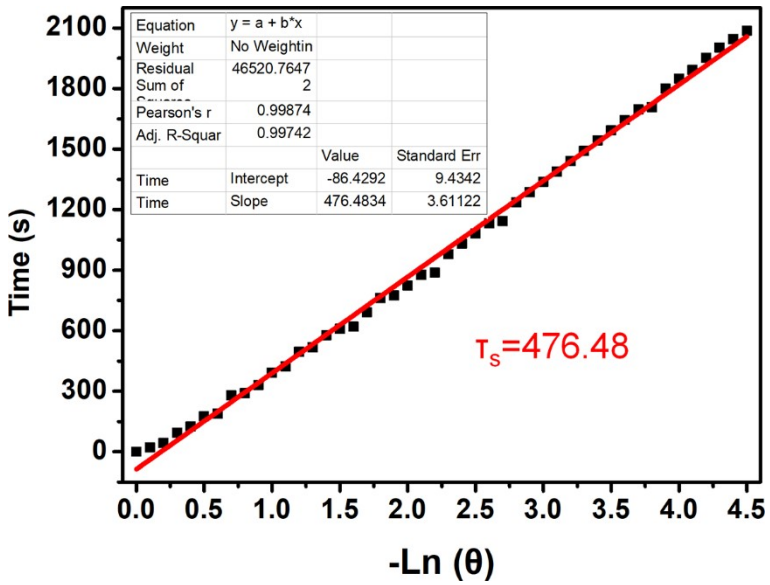

Figure S17. Linear time data from the cooling period versus the negative natural logarithm of driving force temperature of IL-$Ti_3C_2T_x$ MXene nanosheets, giving the value of the time constant as 476.48 s.

Calculation of the photothermal conversion efficiency: The photothermal conversion efficiency (η) was determined using the following equations:[6,7]

$$\eta=\frac{hs(T_{\max}-T_{surr})-Q_O}{I(1-10^{-A_\lambda})}\times 100\% \qquad (3)$$

Where η is the conversion efficiency of 808 nm laser energy to thermal energy. T_{max} is the maximum temperature at equilibrium and T_{surr} is the ambient temperature. Q_o is the baseline energy generated by quartz cells and water upon laser irradiation. I is incident laser power. A_{808} is the absorbance of IL-$Ti_3C_2T_x$ MXene nanosheets at 808 nm. S is the surface area of the cell and h is the heat transfer coefficient. hs is calculated by the following equations:

$$hs = \frac{\sum_i C_{p,i} m_i}{\tau_s} \qquad (4)$$

Where τ_s is the time constant. m and c are the mass and capacity of pure water. Among that, m is 1.989 g and c is 4.2 J g^{-1} K^{-1}. τ_s is 476.48 s (Figure S17), T_{max}-T_{surr} is 35.8 ℃. A_{808} is 1.394, and I is 1.0 W cm^{-2}. Q_0 is 14.2 mW. So, the photothermal conversion efficiency is 63.91%.

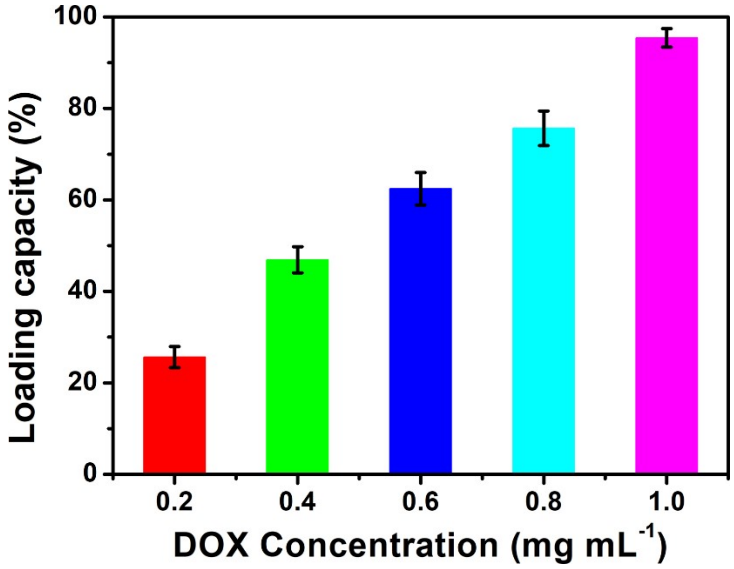

Figure S18. DOX loading capacity of IL-$Ti_3C_2T_x$ MXene nanosheets at various DOX concentrations (n=3).

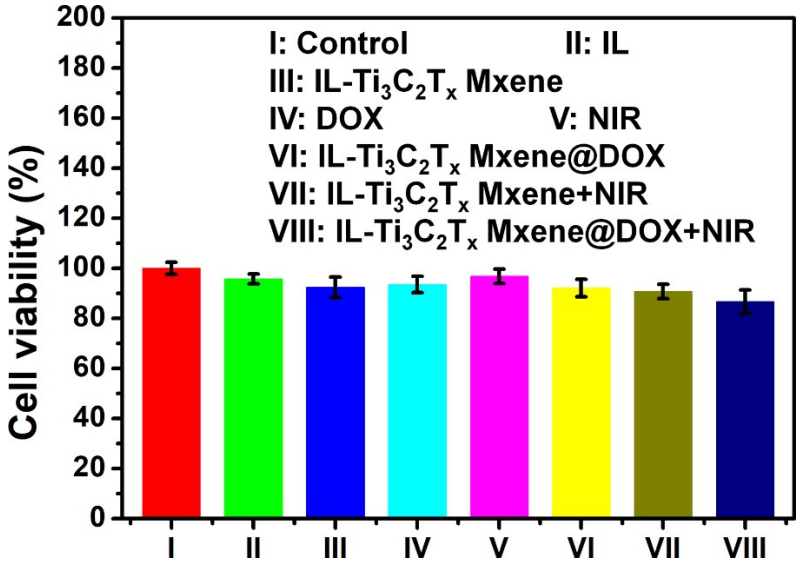

Figure S19. Cell viability of different groups against L929 cells after 24 h incubation (n=6).

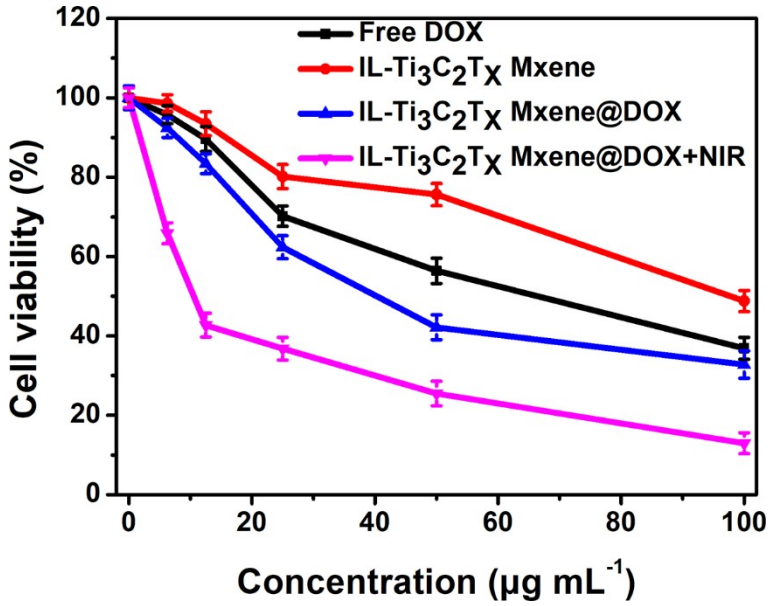

Figure S20. Cell cytotoxicity of free DOX, IL-$Ti_3C_2T_x$ MXene, IL-$Ti_3C_2T_x$ MXene@DOX, IL-$Ti_3C_2T_x$ MXene@DOX+NIR against 4T1 cells after 24 h incubation (n=6).

Table S5. Calculated 50% inhibiting concentration (IC_{50}) of different formulations of free DOX, IL-$Ti_3C_2T_x$ MXene, IL-$Ti_3C_2T_x$ MXene@DOX, IL-$Ti_3C_2T_x$ MXene@DOX+NIR against 4T1 cells (n=6).

Sample	IC_{50} (μg mL^{-1})
	4T1 cells
Free DOX	67.31±3.26
IL-$Ti_3C_2T_x$ MXene	97.45±3.89
IL-$Ti_3C_2T_x$ MXene@DOX	40.62±2.87
IL-$Ti_3C_2T_x$ MXene@DOX+NIR	10.48±2.03

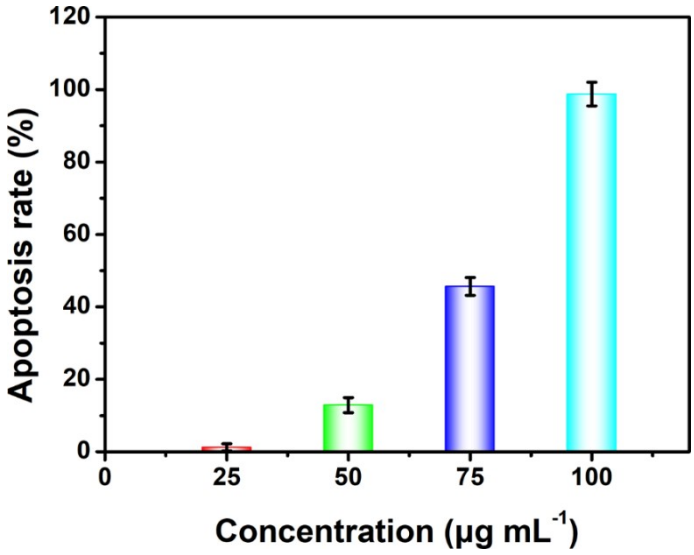

Figure S21. Relationship between apoptosis and concentration of IL-$Ti_3C_2T_x$ MXene nanosheets (n=3).

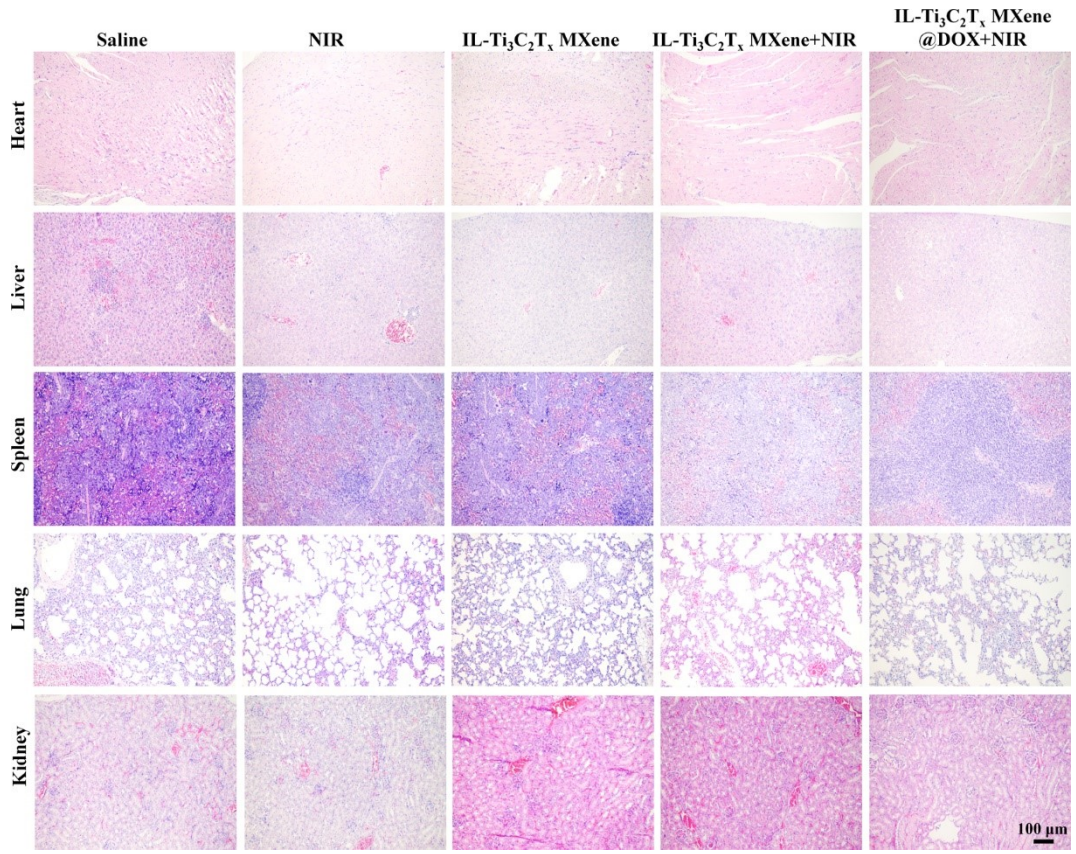

Figure S22. H&E staining of major organs (heart, liver, spleen, lung, and kidney) of 4T1 tumor-bearing mice after various treatments (scale bars: 100 μm).

References

1. F. Chen, Y. Y. Ren, J. N. Guo, F. Yan, *Chem. Commun*., 2017, **53**, 1595-1598.
2. B. B. Lu, Y. B. Li, Z.Y. Wang, B. S. Wang, X. Pan, W. W. Zhao, X. Ma, J. H. Zhang, *N. J. Chem*., 2019, **43**, 12275-12282.
3. Y. Y. Ma, X. F. Lv, D. B. Xiong, X. S. Zhao, Z. H. Zhang, *Appl. Catal. B: Environ*., 2021, **284**, 119720-119733.
4. Q. W. Yang, D. Xu, J. Z. Zhang, Y. M. Zhu, Z. G. Zhang, C. Qian, Q. L. Ren, H. B. Xing, *ACS Sustainable Chem. Eng*., 2014, **3**, 309-316.
5. Z. Y. Wang, J. C. Zhang, B. B. Lu, Y. B. Li, Y. H. Liang, J. M. Yuan, M. Zhao, B. S. Wang, K. Mai, J. H. Zhang, *J. Mol. Liq*., 2019, **296**, 111822-111828.
6. G. Y. Liu, J. H. Zou, Q. Y. Tang, X. Y. Yang, Y. W. Zhang, Q. Zhang, W. Huang, P. Chen, J. J. Shao, X. C. Dong, *ACS Appl. Mater. Interfaces*, 2017, **9**, 40077-40086.
7. T. J. Zhou, X. L. Liang, P. F. Wang, Y. Y. Hu, Y. F. Qi, Y. S. Jin, Y. Du, C. H. Fang, J. Tian, *ACS Nano*, 2020, **14**, 12679-12696.